ACS Sustainable Chemistry & Engineering

Research Article

pubs.acs.org/journal/ascecg

Ultralow Thermal Conductivity Minimum in Silicon Supercrystals with Weakly and Strongly Bonded Germanium Nanodots for Thermoelectrics

Jean-Numa Gillet*

School of Computational and Integrative Sciences (SCIS), Jawaharlal Nehru University (JNU), New Mehrauli Road, New Delhi, 110067, India

Supporting Information

ABSTRACT: An ultralow thermal conductivity showing a minimum of the order of 0.01 W/(m K) is predicted at T = 300 K in a Si/Ge quantum dot crystal with a Ge nanodot spacing d = ±30 nm. This theoretical result is obtained when all Ge nanodot interfaces are assumed to be weakly bonded with respect to the Si matrix. The thermal conductivity is a decreasing functional of the weakly bonded nanodot density q, defined as the number of weakly bonded dots divided by the total number of dots in the Si/Ge supercrystal. The thermal conductivity minimum for a given q is reached when d is increased to the optimal period d*. When only one nanodot out of six is weakly bonded (case of q = 1/6), the thermal conductivity of air (±0.025 W/(m K)) is already reached. A high thermoelectric figure of merit ZT is envisioned. Indeed, ZT depends on the inverse of the thermal conductivity, which may present ±15 000-fold reduction compared with that of bulk Si (case of q = 1). The ±1 W/(m K) mark could not be significantly beaten using nanomaterials with phonon blocking properties presenting a lower dimensionality than 3, in contrast to the supercrystal with weak bonds.

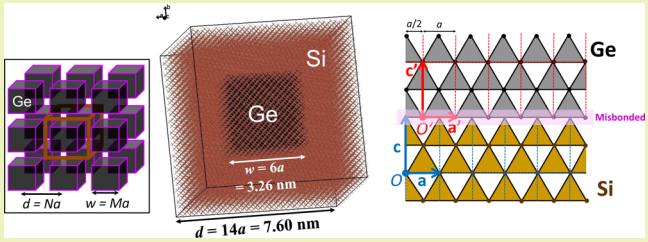

KEYWORDS: *Molecular modeling, Green energy materials, Nanomaterials, Thermoelectrics, Alternative energy*

INTRODUCTION

If S, σ, and T respectively denote the Seebeck coefficient, electrical conductivity, and temperature, the thermoelectric figure of merit $ZT = S^2\sigma T/\lambda$ is proportional to the power factor $S^2\sigma$ but depends on the inverse of the thermal conductivity λ. Significant renewable energy progresses would be obtained if a high ZT > 2 or 3 could be reached. If the thermal contact resistances could be avoided, $ZT \geq 3$ would produce a thermoelectric yield higher than 42% of the Carnot efficiency (for hot and cold junctions at 800 and 300 K, respectively). Such efficiency is competitive with the yields of conventional thermal engines. Therefore, the design of semiconducting nanomaterials showing an ultralow lattice thermal conductivity is an active research area of alternative energy science and engineering.[1−12] Semiconductors with an indirect electronic band gap are also preferred to avoid the electronic part λ_e of the thermal conductivity.

Superlattices were first studied to achieve ZT > 1 owing to λ reduction between their thin periodic layers. However, their synthesis with ZT > 1 is usually not possible due to lattice mismatches forming dislocations and cracks. Nanowires were as well proposed for one-dimensional (1D) phonon confinement owing to the quasi 0 dimensionality of the directions orthogonal to the longitudinal axis.[8,9] In experiments, these 1D insulating nanomaterials usually fail to beat the lowest thermal-conductivity limit $\Lambda_{min} \approx$ 1 W/(m K) of bulk amorphous Si.[9−12] Three-dimensional (3D) nanostructured materials are potentially better to reduce λ due to enhanced confinement of the phonons inside a 3D-type barrier.[1,13,14]

Novel epitaxial and self-assembly technologies (as nanoscale molecular beam epitaxy) have been used for bottom-up synthesis of many types of nanomaterials.[1,13,15] For instance, 3D Ge quantum dot arrays in a Si matrix were synthesized for quantum-device and solar-energy applications.[16,17] As illustrated in Figure 1, a Si/Ge supercrystal molecular structure is proposed by supercell repetition. From this theoretical model, we show that 3D high-density Ge quantum dot arrays in Si could also present an ultralow thermal conductivity, possibly leading to high ZT. The calculated extreme λ reduction is due to two distinct phenomena: The first decrease factor is "coherent" and comes from the low phonon group velocities derived from the folded dispersion diagram computed by lattice dynamics.[1,4] On the other hand, $\lambda \sim$ 0.05 W/(m K) was experimentally measured in two-dimensional (2D) layered WSe_2 crystals presenting weak covalent bonding at their layer interfaces.[11] By analogy with these experiments and others,[12] weak covalent bonding of the Ge nanodots−Si matrix interfaces is introduced in the Si/Ge supercrystal, resulting in an

Received: November 13, 2012
Revised: March 25, 2013
Published: April 2, 2013

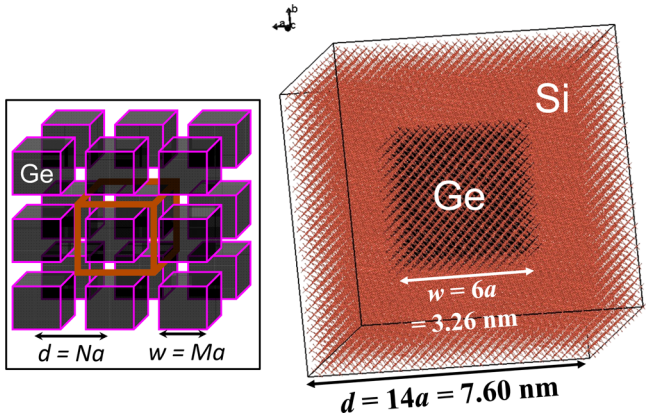

Figure 1. Si/Ge supercrystal with $N = 14$ and $M = 6$. The parameters of the Ge nanodots located at the supercell centers are the following: spacing $d = 14a = 7.6034$ nm and width $w = 6a = 3.2586$ nm. 2198 Ge atoms and 19 754 Si atoms are respectively denoted by black and brown balls and sticks to form a supercell. (left inset) Continuous supercrystal view at a larger scale forming a "phononic crystal" motif.

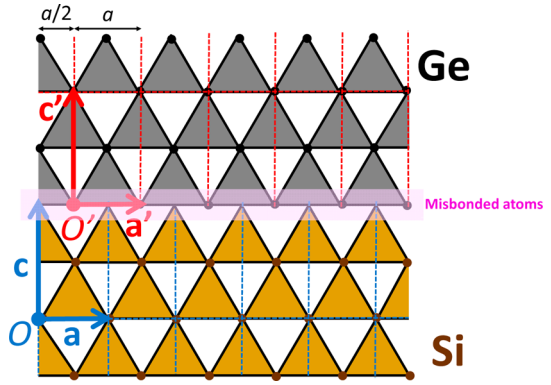

Figure 2. Simplified 2D projection: Si/Ge interface with misbonded atoms at the separation between the two materials. A tetrahedron, with one atom at its center of mass that is covalently bonded to four other atoms located at its corners, is typical of the dc group. In this 2D figure, c is the primitive vector that is supposed to be orthogonal to the bottom Si epitaxial layer (with the lattice sites depicted as dark brown dots). We also project a sp^3 tetrahedron to form an equilateral triangle with three atoms at its corner. In addition, we assume that the Ge nanocrystal lattice sites (denoted as black dots) are shifted by $f_1 a$ (with $f_1 = 1/2$) in the direction of the primitive vector **a** compared with the Si matrix, so that the origin O' of the local symmetry axes **a**′ and **c**′ of the Ge nanodot is translated by the distance $a/2$ in the same direction. The Si/Ge separation is highlighted using a thin transparent rectangle of pink color (in the middle). We observe that the light brown triangles of the Si matrix, in the layer just below the separation, are not connected at their corners to the gray triangles of the Ge nanocrystal, in the layer just above. The Ge nanodot is therefore weakly bonded to the Si matrix due to the absence of correct covalent bonds between the two materials at their interface. Nonexistence of covalent bonds can as well occur between the Ge and Si atoms at the separation.

additional λ decrease effect. Indeed, phonon scattering is not coherent, at the misbonded interfaces, with the utilized Stillinger–Weber potential in conjunction with the Umklapp scattering process (U process), at the infinite supercrystal scale. Hence, an additional scattering relaxation time is computed using an incoherent model of phonon near-field scattering by the weakly bonded Ge nanodots and has to be added to the usual U process probability in agreement with the Boltzmann transport equation (see the Supporting Information). In the incoherent model, the scattering cross section is set to the geometrical limit of the misbonded scatterer according to scattering in near-geometrical optics (as explained in the next sections). The terminology incoherent is preferred because we believe that the 3D misbonded barriers could generate significant nonfocusing of the phonons, if they could be experimentally observed as the photons in optics.

In this report, we especially focus on the λ dependence vs the number of weakly bonded nanodots in the Si/Ge supercrystal. An important parameter to be considered in this analysis is the density q of weakly bonded Ge nanodots, defined as the number of weakly bonded nanodots divided by the total number of nanodots in the overall supercrystal, designed with both weakly and perfectly bonded dots. In an epitaxial process, we could consider **c** as the primitive vector along the growth axis of a Ge nanodot, which is orthogonal to an Si epitaxial layer with the in-plane crystallographic axes related to the primitive vectors **a** and **b**, defined at a reference lattice site O. Inside a space that can be as small as one monolayer, weak covalent bonding of a Ge nanoparticle with the local symmetry axes **a**′, **b**′, and **c**′ can be induced by translation of the lattice sites of the nanodot, in the directions **a** and **b**, with respect to those of the Si matrix. After translation, the reference lattice site O' of the nanodot local axes is shifted by $f_1 a$ and $f_2 b$ compare to O, in the directions of the vectors $\mathbf{a} = a\mathbf{1}_a$ and $\mathbf{b} = b\mathbf{1}_b$, respectively, where f_1 and f_2 are fractional numbers lower than 1. As shown in two dimensions in Figure 2, the largest translation is obtained for $f_1 = f_2 = 1/2$ in the diamond-cubic (dc) symmetry. This transformation leads to failure of the tetrahedral sp^3 covalent bonding structure at the Ge nanodot–Si matrix interfaces of the Si/Ge supercrystal. For one interface, the tetrahedrons are represented by equilateral triangles in the 2D simplified projection in Figure 2. These Si/Ge interfaces become weakly bonded due to both incorrect and missing Ge–Si covalent bonds that occur at their separations thereof. Phonon incoherent scattering by the misbonded interfaces could be significant because the interfacial lack of proper covalent bonds creates 3D vibration-mode transport barriers and they cannot propagate in the quantum dots.

From the precedent, phonon scattering in the Si/Ge supercrystal is of two types: (i) coherent due to the low group velocities leading to localization and (ii) incoherent due to the misbonded interfaces resulting in nonfocusing. The incoherent effect therefore is a second factor on the huge λ decrease (additional to the low-group-velocity effect). When all Ge nanodots are weakly bonded ($q = 1$), a fast λ diminution is first observed when the nanodot spacing d [Figure 1] is augmented in the supercrystal. A global minimum $\lambda^* = 0.009$ W/(m K) of the supercrystal thermal conductivity, corresponding to a 17 000-fold decrease with respect to bulk Si (~150 W/(m K)), is computed at $T = 300$ K when d reaches the optimal value $d^* \approx 30$ nm (according to the proposed model). A high $ZT > 1$ is envisioned from this result. After the minimum is obtained, the λ curve increases above Λ_{min} for d larger than ~500 nm in Si/Ge supercrystals with a ~ 12.5 Ge at % filling ratio in the Si matrix.

THEORETICAL METHOD

Supercrystal Structure. The ultralow λ in the Si/Ge supercrystal is investigated from a 3D supercell model. A nanostructures looking like a 3D phononic crystal, if the medium were continuous, is obtained. The supercrystal lattice

dx.doi.org/10.1021/sc400020c | ACS Sustainable Chem. Eng. 2013, 1, 611–618

parameter $d = Na$ is given in the ⟨100⟩ directions by an integer number of interatomic distances denoted by a, as shown in Figure 1. A cubic supercell is composed of $N \times N \times N = N^3$ dc cells with eight atoms per primitive cell and is repeated to obtain a simple-cubic (sc) supercrystal at the "phononic crystal" scale [inset of Figure 1]. If $N = 14$, a supercell contains $N^3 = 2774$ dc cells and $8N^3 = 21\,952$ atoms. In each supercell, the Si atoms in a central subset of $M \times M \times M = M^3$ dc cells are substituted by Ge atoms to form a nanodot with the edge length $w = Ma$ in ⟨100⟩. If $N = 14$, $N - 1 = 13$ cubic-nanodot configurations are accepted (by definition) because the nanodot basis in number of a interatomic distances can vary from $M = 1$ to $M = N - 1 = 13$. The $N - 1 = 13$ possible Si/Ge supercrystal types with $N = 14$ present the same nonrelaxed nanodot spacing $d = Na = 14a = 7.6034$ nm. However, $M = 6$ corresponds to the nanodot basis $w = Ma = 6a = 3.2586$ nm (possible if $N \geq 7$). When $M = 3$, 6, or 9, each nanodot respectively contains $n_{Ge} = 344$, 2198, or 6860 Ge atoms and is surrounded by $n_{Si} = 21\,608$, 19 754, or 15 092 Si atoms in a supercell with $N = 14$. In Figure 1, the Ge and Si atoms are respectively depicted by black and brown sticks and balls ($N = 14$), according to the sp^3 covalent structure. The supercrystal with $N = 14$ and $M = 6$ has a chemical composition Ge_xSi_{1-x} given by the Ge nanodot filling ratios $x = 2198/19\,754 \approx 11.1$ Ge at %. Here, x is set to the mean value of ~1/8 = 12.5 Ge at %.

Thermal Conductivity. Due to the low dimensions of the nanoscale embedded scatterers (see Supporting Information), the lattice thermal conductivity of the supercrystal can be computed by integration over the only radial wavenumber $k = |\mathbf{k}|$ as

$$\lambda = \frac{1}{3}\sum_{m=1}^{N_m}\int_0^{k_{max}} \tau_m(k)[v_m(k)]^2 \hbar\omega_m(k)\frac{\partial n_m^{(0)}(k)}{\partial T}\kappa(k)\,dk \quad (1)$$

In eq 1, $\hbar$ is the reduced Planck constant. The index $m = 1$ to N_m designates one branch of the N_m dispersion curves $\omega_m(k)$ obtained by lattice dynamics with the Stillinger–Weber force field.[18] The phonon group velocities $v_m(k) = d\omega_m(k)/dk$ are computed by derivation of the dispersion curves with respect to k. The number of eigenmodes is given by $N_m = 3 \times 8N^3 = 24N^3 = 65\,856$ for the $N - 1 = 13$ possible supercrystals with $N = 14$ [Figure 1]. In eq 1, the phonon scattering relaxation times $\tau_m(k)$ and Bose–Einstein distributions $n_m^{(0)}(k)$ for a temperature T are all functional of k. The kernel $\kappa(k)$ is adjusted to obtain the same thermal conductivity than that of bulk Si when the Si matrix does not contain any nanodot ($M = 0$), as explained in the Supporting Information. The 1/3 multiplying factor is the result of this adjustment and in agreement with the kinetic theory for the thermal conductivity. The integral in eq 1 is calculated over the finite interval $[0, k_{max}]$, where the maximum k value, k_{max}, is located at the right border of the first Brillouin zone (BZ1). For a bulk dc material with $3 \times 2 = 6$ dispersion curves, this boundary is located at $k_{max} = 2\pi/a$ with $a = 0.5431$ nm for bulk dc Si. In contrast, in a Si/Ge supercrystal with the nanodot spacing $d = Na$, $k_{max} = \pi/d$ is used in eq 1 due to the sc crystallinity at the "phononic crystal" scale. When $N = 14$, BZ1 is divided by $2N = 28$ folds with respect to that of bulk dc Si because $(2\pi/a)/(\pi/d) = 2d/a = 2N$.

Umklapp and Near-Field Scattering. For a perfect supercrystal (with a perfect bonding structure, i.e. $q = 0$), only the U process relaxation time $\tau_m^{(u)}(k)$ of the modes (m, k) is considered to compute λ with $\tau_m(k) = \tau_m^{(u)}(k)$ in eq 1. An analytical expression was used by a number of authors to calculate $\tau_m^{(u)}(k)$ vs T.[4,19−21] To model the second factor on the extreme λ reduction in the Si/Ge supercrystal, weak bonding at the interfaces between a number of Ge nanodots (with the density q) and the Si matrix is introduced by the incoherent or near-field scattering relaxation time $\tau_m^{(q)}(k)$. Here, λ is computed in supercrystals containing both weakly and perfectly bonded nanodots. λ is analyzed vs the density q between 0 and 1. The total relaxation time $\tau_m(k)$ is obtained by addition of two time-scattering probabilities as

$$[\tau_m(k)]^{-1} = [\tau_m^{(u)}(k)]^{-1} + [\tau_m^{(q)}(k)]^{-1} \quad (2)$$

Scattering independence[22] is considered between the scatterers corresponding to the weakly bonded nanodots with a density q in the supercrystal. A priori, multiple scattering and defects would lead to an even lower λ than that computed in this study [by addition of other time probability terms in eq 2]. However, if the density of defects would become too high, the thermal conductivity could be higher and increase above Λ_{min} because the nanomaterial would not behave anymore as a weakly bonded supercrystal with 3D barriers but as an amorphous bulk material.[11] For $q \neq 0$ and $q \neq 1$, disorder effects are already included in the term $1/\tau_m^{(q)}(k)$ in eq 2. Indeed, the weakly bonded nanodots can be chosen randomly in the total crystal with a density q that is not related to their individual positions.

On the basis of classical near-geometrical scattering theory in optics,[23−25] the incoherent probability $1/\tau_m^{(q)}(k)$ is proportional to the average near-field scattering cross section $\bar{\sigma}_q$ over the weakly bonded nanodots as

$$1/\tau_m^{(q)}(k) = \bar{\sigma}_q v_m(k)/V \quad \text{with } \bar{\sigma}_q = 2Gq \quad (3)$$

In eq 3, $V = d^3$ is the supercell volume.[22] Equation 3, for the near-field scattering cross section $\bar{\sigma}_q$, holds for several reasons: First, coherent diffraction, as known in optics,[26−28] is impossible because the average mean free path (MFP) $l_{Si} \sim 100$ nm of the phonons in bulk dc Si remains quite large in comparison with the scatterer separation d, leading to many random collisions and much smaller MFP in the nanostructure. Second, Rayleigh or far-field scattering (in k^4 or ω^4) is negligible for the THz scale folded modes in the Si/Ge nanostructure, even for a small d.[4,23] Indeed, at the local scale of a weakly bonded interface and after unfolding of the dispersion diagram (global scale), most of the "optical" modes have unfolded scattered wavelengths smaller than the system characteristic size (~d), leading to near-field scattering. Note that the wavelength at the BZ1 boundary is calculated as $2\pi/k_{max} = 2d$. In addition, the three "acoustical" modes (starting from the 0 frequency) represent less than $3/(24N^3) = 0.005\%$ of the folded BZ1 occupancy when $N \geq 14$. However, it was shown in refs 4 and 23 that the phonon scattering cross section quickly grows to the geometrical limit ($2G$) within BZ1 and thereafter shows damped oscillations around this limit in the higher order Brillouin zones for the unfolded wavenumbers $k > k_{max}$ (see, for example, Figure 4 in ref 4), in agreement with scattering in optics.[24,25] From the precedent, the cross section $\bar{\sigma}_q$ is assigned to its geometrical limit $2G$ for one misbonded nanodot, which seems to be a reasonable approximation.

When all nanodots in the supercrystal are weakly bonded, the effective cross section is given by $\bar{\sigma}_q = 2G$ because $q = 1$ in eq 3. $G = \pi R^2$ in eq 3 is the geometrical projection of one of the weakly bonded nanodots with the average equivalent radius R.

dx.doi.org/10.1021/sc400020c | ACS Sustainable Chem. Eng. 2013, 1, 611−618

This surface has to be multiplied by 2 (extinction paradox) to obtain $\bar{\sigma}_q$ for $q = 1$ in eq 3.[24,25] However, when $q < 1$, the final expression [eq 3] for the effective cross section is $\bar{\sigma}_q = 2Gq$ by averaging over the only misbonded dots (since we consider scattering independence between the scatterers). The probability $1/\tau_m^{(q)}(k)$ is maximal when $q = 1$ in eq 3, and the lowest λ vs q is obtained for this q value [eqs 1 and 2]. In contrast, the number of weakly bonded nanodots is 0 for a perfect crystal resulting in $1/\tau_m^{(q)}(k) = 0$ because $q = 0$ in eq 3. In this case, only Umklapp scattering is taken into account because $\tau_m(k) = \tau_m^{(u)}(k)$ from eq 2. The largest λ vs q is therefore obtained when $q = 0$ [eqs 1 and 2]. Density values within the interval $0 < q < 1$ are intermediate cases with a partial number of weakly bonded nanodots. λ significantly decreases when q is increased from 0 to 1. Note that $\tau_m^{(u)}(k)$ is computed from a traditional analytical expression.[20] This model holds in the nanostructure since the average MFP due to Umklapp scattering l_u remains of the order of that of bulk Si, $l_{Si} \approx 100$ nm.[4] However, the average MFP l_q from the weakly bonded nanodot interfaces, due to $\tau_m^{(q)}(k)$, is of the order of 10 nm or less.[14] Consequently, l_q is predominant over l_u and the total average MFP l is closed to l_q. The term l_u has to be seen as a reference value to compute the only coherent effect of the low phonon group velocities when all nanodot interfaces are correctly bonded with the Si matrix (case of the perfect crystal with $q = 0$).

RESULTS AND DISCUSSION

Dispersion Curves. Figure 3a presents a number of the $24N^3 = 65\,856$ dispersion curves of the Si/Ge supercrystal with $N = 14$ and $M = 6$ [Figure 1]. The 30 first dispersion curves related to the phonon eigenmodes from $m = 1$ to 30 in a frequency range of 1.08 THz, from $f_1(0) = 0$ THz to $f_{30}(0) \approx 1.08$ THz, are displayed by the 30 bottom black lines (where $f_m(k = 0) = \omega_m(k = 0)/2\pi$ are the phonon eigenfrequencies for the $k = 0$ wavenumber). Above them, the dispersion curves depicted by orange lines correspond to a selected number of the 600 branches corresponding to eigenmodes between $m = 31$ and 630 in a frequency interval of 1.5 THz, from $f_{31}(0) \approx 1.08$ THz to $f_{630}(0) \approx 2.58$ THz. A chosen number of the $65\,856 - 30 - 600 = 65\,226$ remaining dispersion curves with the highest frequencies are related to the blue lines and plotted in a frequency band from $f_{631}(0) \approx 2.58$ THz to $f_{65\,856}(0) \approx 20$ THz. As observed in Figure 3a, the dispersion curves are usually quite flat and become even flatter when the angular frequency $\omega_m(k)$ is increased with a higher m value. Their slopes, related to the amplitudes of the phonon group velocities $v_m(k)$ in eq 1, are therefore quite small ($v_m(k) = d\omega_m(k)/dk$). A first coherent effect on the extreme reduction of the thermal conductivity in eq 1 results from this phenomenon. Mention that, for the same supercrystal size parameters N and M, the same set of dispersion curves is computed for the strongly ($q = 0$) and weakly ($q > 0$) bonded nanostructures. Recall that $N \geq 14$ already corresponds to a number of dispersion curves larger than 65 856 including many higher-frequency branches with a quite flat behavior. In addition, the folded dispersion diagram can be computed only at the scale of the whole "phononic" crystal. Owing to these two reasons, the dependence of the band structure with respect to q is of second order and can be neglect, already for small N values.

Figure 3b is a close-up of the bottom of Figure 3a, displaying all the 630 dispersion curves related to the eigenmodes from $m = 1$ to 630 located in a low frequency band from $f_1(0) = 0$ THz to $f_{630}(0) \approx 2.58$ THz. The 30 bottom branches from $m = 1$ to

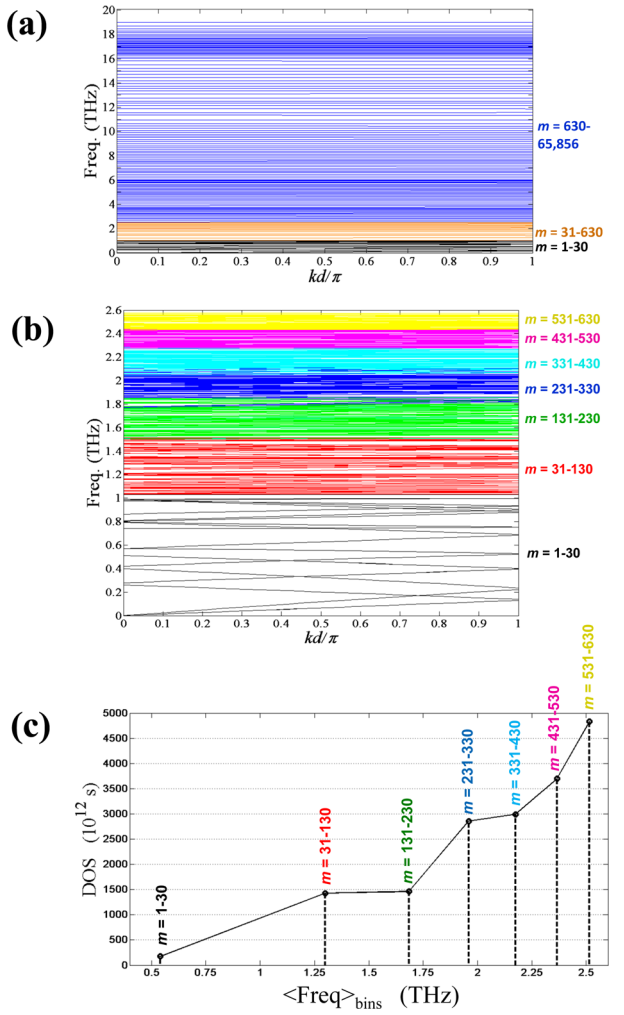

Figure 3. (a) Chosen branches of the dispersion diagram of the Si/Ge supercrystal with $N = 14$ and $M = 6$. (b) Close-up of the 630 dispersion curves with the lowest frequencies in the range from 0 to 2.58 THz. (c) Density of states (DOS) in the range from 0 to 2.58 THz. The seven bin sizes to obtain the DOS correspond to the bandwidths containing the dispersion curves colored in black ($m = 1$ to 30), red ($m = 31$ to 130), green ($m = 131$ to 230), blue ($m = 231$ to 330), cyan ($m = 331$ to 431), magenta ($m = 431$ to 530), and yellow ($m = 531$ to 630) in part b.

30 are first drawn in part b using black lines in a frequency interval from $f_0(0) = 0$ THz to $f_{30}(0) \approx 1.08$ THz. In the full dispersion diagram, shown in part a, they were depicted by the 30 bottom lines with the same black color. In part b, the 600 dispersion curves indexed by $m = 31$ to 630 inside a higher frequency range with a width of 1.5 THz from $f_{31}(0) \approx 1.08$ THz to $f_{630}(0) \approx 2.58$ THz are sketched within six frequency intervals using a set of multiple colors. In the full dispersion diagram in part a, a number of these curves were plotted using a unique orange color. In part b, each of the 6 higher-frequency intervals contains 100 dispersion curves each. They are depicted by red, green, blue, cyan, magenta, and yellow lines and respectively related to the branches from $m = 31$ to 130, 131 to 230, 231 to 330, 331 to 430, 431 to 530, and 531 to 630 [Figure 3b]. After observation of the groups of the 600 dispersion curves sketched with multiple colors in part b, we can see that their slopes (giving the group velocities) tend to decrease with an increasing frequency. The 30 bottom branches in black color for $m = 1$ to 30 present the largest slopes in

dx.doi.org/10.1021/sc400020c | ACS Sustainable Chem. Eng. 2013, 1, 611−618

Figure 3b and are included in a quite large frequency band of Δf_{black} = 1.08 THz. In contrast, the 100 dispersion curves in red color for m = 31 to 130 are contained in a smaller frequency interval with a bandwidth Δf_{red} = 0.44 THz, less than half of that (Δf_{black}) in which the 30 bottom black-colored curves are drawn. In addition, the number of the black-colored branches is lower by ∼3.3-fold with respect to that of the red-colored curves [Figure 3b], resulting in a higher density of states (DOS) in Δf_{red} compared with that in the bandwidth Δf_{black}. Above the frequency range Δf_{red} (containing the 100 red-colored branches), the 5 other higher-frequency intervals in part b, Δf_{green}, Δf_{blue}, Δf_{cyan}, $\Delta f_{magenta}$, and Δf_{yellow}, with dispersion curves respectively sketched in green, blue, cyan, magenta, and yellow colors, have decreasing bandwidths for an increasing frequency but for the same number of 100 dispersion curves per interval, leading to a growing DOS with the frequency. In the top of Figure 3b, the 100 yellow-colored curves are in a frequency interval of only Δf_{yellow} = 0.13 THz (from $f_{531}(0) \approx 2.45$ THz to $f_{630}(0) \approx 2.58$ THz). This band is the smallest compared with the increasing bandwidths $\Delta f_{magenta}$ = 0.17, Δf_{cyan} = 0.21, Δf_{blue} = 0.22, Δf_{green} = 0.43, Δf_{red} = 0.44, and Δf_{black} = 1.08 THz of the six frequency intervals that contain the dispersion curves respectively depicted in magenta, cyan, blue, green, red and black colors, from the top (higher frequencies) to the bottom (lower frequencies) of part b.

Figure 3c shows the DOS obtained from the previous band-diagram analysis of the 630 modes with the dispersion curves drawn in part b, from $f_0(0)$ = 0 THz to $f_{630}(0) \approx 2.58$ THz. The DOS g is computed as $g(\Delta\omega) = D(\Delta\omega)/\Delta\omega$, where $D(\Delta\omega)$ is the number of eigenvalues $\omega_m(0)$ in a angular frequency bin $\Delta\omega = \omega_s(0) - \omega_r(0)$ with the mode index m in the interval $r \le m \le s$ (r and s are positive integers). In practice, we compute the DOS using the seven frequency bins Δf_{black}, Δf_{red}, Δf_{green}, Δf_{blue}, Δf_{cyan}, $\Delta f_{magenta}$, and Δf_{yellow}, displayed in part b, as

$$g(\Delta\omega_{bin}) = D(\Delta\omega_{bin})/\Delta\omega_{bin} \quad \text{with } \Delta\omega_{bin} = 2\pi\Delta f_{bin} \tag{4}$$

In eq 4, the index bin corresponds to "black", "red", "green", "blue", "cyan", "magenta", or "yellow" in the color indexation of part b. $D(\Delta\omega)$ = 30 in the bin Δf_{black}, and $D(\Delta\omega)$ = 100 in the six higher-frequency bins with the dispersion curves plotted in red, green, blue, cyan, magenta, or yellow in Figure 3b. Hence, we obtain seven values for the DOS in part c, where the frequency coordinate for each DOS value is taken at the middle of the related bin. We observe a nonlinear increase of the DOS for an increasing frequency.

From normal to high temperatures, the summation in eq 1 has to be performed over all eigenmodes (from m = 1 to $24N^3$ = 65 856 when N = 14) in a frequency range from 0 to 20 THz. Indeed, although the slopes of the dispersion curves related to the $|v_m(k)|$ amplitudes in eq 1 tend to decrease for an increasing frequency, the DOS tends, in contrast, to grow for an increasing frequency. Consequently, the "optical" modes of higher frequencies cannot be neglect in the summation over m in eq 1. Moreover, according to Planck 's law, the population of the many "optical" modes tend to increase with T. We therefore obtained an even lower thermal conductivity for T > 300 K since the high-frequency modes with low group velocities became more populated.[14]

Ultralow Thermal Conductivity Minimum. Figure 4 shows evolutions of λ vs $d = Na$ at T = 300 K. The X and Y axes correspond to $\log_{10}(d)$ and $\log_{10}(\lambda)$, respectively. The seven

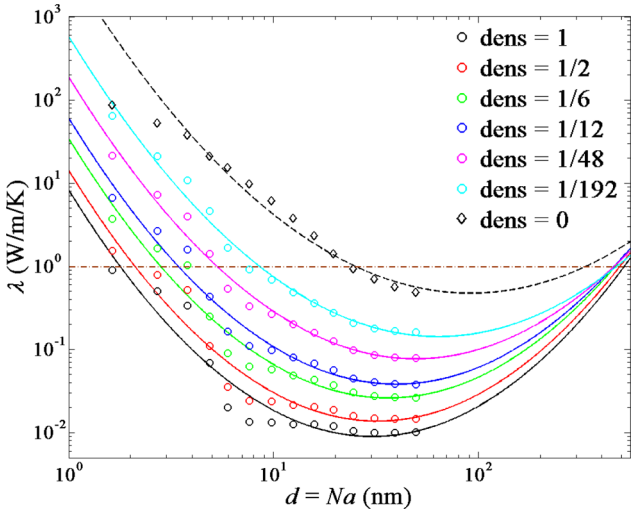

Figure 4. Thermal conductivity λ vs nanodot spacing d curves for seven values of the density q. From the bottom to top, the black, red, green, blue, magenta, and cyan solid curves, fitting the circles with the same color, are respectively computed for q = 1, 1/2, 1/6, 1/12, 1/48, and 1/192. The black dashed curves, fitting the diamonds of the same color, corresponds to the perfect crystal with q = 0. The brown dashed−dotted horizontal line is a reference to Λ_{min} for amorphous Si.

interpolation curves, sketched using multiple colors, are computed for seven chosen q values between q = 0 and 1 in Si/Ge supercrystals with $x \approx$ 12.5 Ge at %. The bottom solid black line displays the λ vs d interpolation curve assuming that all nanodots are weakly bonded in the supercrystal (q = 1). The near-field scattering cross section is therefore maximal because q = 1. From the leftmost to rightmost parts of Figure 4, the vertically aligned circles and diamonds of multiple colors are computed for supercrystal parameters increasing from N = 3 to 91 for the nanodot spacing and from M = 1 to 45 for their basis. Fourteen supercrystals modeled with q = 1 are related to the black-colored circles. These points are fitted (in the double log scale) by the black solid curve using a quadratic interpolation of log λ vs log d [bottom of Figure 4]. Indeed, by observation of the black solid curve (q = 1), a linear decrease of this curve is first obtained for the supercrystals composed of the smallest-size nanodots, from a proportionality with the negative of the supercell-volume (V) logarithm. However, when d > 5.97 nm (N > 11 and M > 5), the solid black curve decreases at a slower pace until a global minimum λ^* = 0.009 W/(m K) of the thermal conductivity is reached for q = 1.

The ultralow thermal conductivity λ^* shows an extreme reduction of ∼17 000 folds compared with that of bulk Si. The term $\lambda^*(q = 1)$ is obtained for the nanodot spacing $d = d^*$ = 30.4 nm corresponding to the nanodot size $w = w^*$ = 14.7 nm. These d^* and w^* optimal values are related to the integer size parameters N = 56 and M = 27, respectively. When $d > d^*$, the black solid curve grows to finally pass Λ_{min}. This curve increases above Λ_{min} when $d \ge$ 500 nm after its extrapolation for large d values [right part of Figure 4]. A nanodot separation larger by at least 5-fold with respect to the MFP $l_{Si} \approx$ 100 nm is necessary to find back a macroscopic effective medium for thermal transport. A nanodot basis w < 250 nm must therefore be used to beat Λ_{min} in supercrystals with q = 1.

The utilized fit results in $\log \lambda = c_2X^2 + c_1X + c_0$, where X = log d and the coefficients c_0, c_1, and c_2 correspond to the lowest root-mean-square deviation (RMSD) between the black circled

dx.doi.org/10.1021/sc400020c | ACS Sustainable Chem. Eng. 2013, 1, 611−618

points and interpolation curve. First, when X is small, log λ presents a quasilinear diminution with X. Indeed, in this case, λ decreases in d^{c_1}, where c_1 is in a range between −3 and −2. c_1 = −3 would mean that λ diminishes with the inverse of V. For larger X values, the log λ vs X curve flattens. Therefore, a second-order correction c_2X^2 has to be added to the initial linear polynomial $\log \lambda \approx c_1X + c_0$. A quadratic instead of cubic polynomial (with four instead of only three fitting coefficients) of X is chosen to interpolate log λ. Indeed, a smaller RMSD is computed for the quadratic polynomial compared with the cubic fit. A quadratic interpolation with only one thermal-conductivity global minimum λ^* is therefore preferred instead of higher order fits in $\sim X^n$. In addition, the quadratic fit leads to $d \geq 500$ nm = $5l_{Si}$ for $\lambda \geq \Lambda_{min}$. The asymptotical value $d \sim 500$ nm of the fit seems reasonable. Indeed, for a supercell width d larger than the MFP $l_{Si} \sim 100$ nm by several folds, one can expect that the nanomaterial loses its phonon-blocking microscopic properties at the misbonded interfaces because the 3D barriers are becoming too large to lead to enhanced phonon scattering.

The seven fits are computed for seven chosen q values. Each curve shows a global minimum $\lambda^*(q)$ depending on q. From the bottom to the top of Figure 4, the black, red, green, blue, magenta, and cyan solid curves are obtained using six decreasing nonzero q values given by q = 1, 1/2 = 0.5, 1/6 = 0.1667, 1/12 = 0.0833, 1/48 = 0.0208, and 1/192 = 0.0052, respectively. In the top of Figure 4, the dashed black curve is a quadratic interpolation of the black diamond points computed for supercrystals with q = 0. Hence, the supercrystals related to the diamonds correspond to perfect crystals and present perfect bonding at all nanodot interfaces. The dashed black fit for q = 0 decreases much more slowly than the solid black curve (q = 1). Indeed, q = 0 corresponds to $\overline{\sigma}_q$ = 0 in eq 3. The dashed black fit (q = 0) reaches its global minimum λ^* = 0.43 W/(m K) when d is increased to d^* = 91.8 nm [Figure 4]. This value remains lower than Λ_{min} by ∼2-fold and is related to the optimal nanodot size w^* = 45.6 nm. The optimal spacing $d^*(q = 0)$ is almost equivalent to l_{Si} because only Umklapp lifetimes have to be considered in eq 1. After the global minimum $\lambda^*(q = 0)$ is reached, the dashed black curve increases above Λ_{min} when $d \geq 300$ nm. Thus, the perfect crystal can as well beat Λ_{min} when $w \leq 150$ nm. Weak covalent bonding at the Si/Ge interfaces is therefore a second (incoherent) effect on the observed extreme λ reduction. Indeed, when q = 1 in the Si/Ge supercrystal, the global minimum $\lambda^*(q = 1)$ shows an additional reduction of $\lambda^*(q = 0)/\lambda^*(q = 1) \approx$ 43-fold with respect to that of the perfect crystal [$\lambda^*(q = 0)$] where the only coherent effect of the low group velocities and Umklapp scattering is considered [eqs 1 and 2]. In addition, the optimal nanodot spacing $d^*(q = 1)$ in the supercrystal with q = 1 is reduced by $d^*(q = 0)/d^*(q = 1) \approx$ 3-fold compared with the perfect crystal [$d^*(q = 0)$]. Indeed, the high number of incoherent scattering events introduced by the maximized $\sigma_m^{(q)}(k) = 2G$ when q = 1 significantly reduces the MFP with respect to the perfect crystal [eqs 2 and 3]. The red, green, blue, magenta, and cyan solid curves are intermediate cases between q = 1 (black solid curve) and q = 0 (black dashed curve) and show global minima respectively given by $\lambda^*(q = 1/2) = 0.013$, $\lambda^*(q = 1/6) = 0.026$, $\lambda^*(q = 1/12) = 0.038$, $\lambda^*(q = 1/48) = 0.078$, and $\lambda^*(q = 1/192) = 0.13$ W/(m K) [Figure 4]. Increases in both λ^* and d^* are observed when q is decreased. The preceding analyses were presented at T = 300 K. However, to obtain a maximized ZT, conventional Si/Ge thermoelectric alloys are used at higher temperatures where a ZT peak occurs.[3] The material stability depends on the lowest melting point of the two constitutive materials (Si and Ge). Therefore, at normal pressure, the proposed Si/Ge nanostructure should as well remain stable and utilizable at high temperatures up to $T \approx$ 1200 K, the last value being the Ge melting point.[14]

Recent experimental measurements in ref 13 showed a thermal conductivity of ∼1 W/(m K) in a Si/Ge quantum dot superlattice. A key point is that the nanostructured Si/Ge crystal experimentally studied by these authors is geometrically different from the Si/Ge supercrystal proposed in our study. First, their Ge nanodots have traditional pyramidal or domelike shapes and are connected together by parallel Ge epitaxial layers on Si spacers. In addition, they present a height that can be smaller by several folds with respect to the Si spacer thickness (due to a low height/width ratio of the nanodots). On the other hand, they can show varying elongations in different crystallographic orientations parallel to a Ge epitaxial layer, after observation of AFM and TEM images.[13] Si/Ge quantum dot superlattices with a comparable geometry than those presented in ref 13 were also fabricated and their thermal conductivity was measured to be as well of the order 1 W/(m K) in the previous literature (see refs 6, 29, and 30, e.g.). From the precedent, with respect to phonon confinement and barriers, the quantum dot superlattice of ref 13 has an effective dimensionality that is not 3D but probably between one and two dimensions. Therefore, its thermal conductivity can be blocked for a given crystallographic direction but can possibly pass in other directions. In ref 1, using a model presenting similarities with that proposed in this paper, thermal conductivity values of ∼1 W/(m K) (as in ref 13) were computed in a 2D Si nanoscale membrane supporting domelike Ge nanodots at its top. In one of the examples, the thickness of the Si nanomembrane was of the same order of magnitude than that of the Si spacer in ref 13. In the nanomembrane, the ∼1 W/(m K) thermal conductivity was obtained in the crystallographic direction were the nanodots have the smallest width.[1] In the orthogonal in-plane direction were the Ge nanodots had an elongated shape, by definition, the directional thermal conductivity was however exalted by more than 20-fold up to ∼30 W/(m K). As a consequence, it was already shown that it is difficult to obtain an overall extreme reduction of the thermal conductivity in nanomaterials that do not possess a fully 3D behavior for phonon blocking and Λ_{min} cannot be beaten by a significant factor, in contrast to this report. Porous Si nanoscale membranes made from thin film technologies were as well-fabricated to reduce the thermal conductivity.[31] However, due to their 2D behavior, these porous membranes cannot be considered as 3D phonon blockers. Hence, as observed in the experimental results in ref 31, Λ_{min} remains the minimal thermal conductivity limit in these materials for the same aforementioned reasons. Also recall mathematically that the free-space DOS to be used in the thermal conductivity integral, as that in eq 1, depends on k^2 in three dimensions but only in k^1 in two dimensions and is a constant (k^0) in one dimension,[1,4,8] in agreement with the precedent.

The weakly bonded nanodot interfaces should not lead to a too significant decrease of the electrical conductivity in comparison with the huge thermal conductivity reduction (to obtain a high ZT). In the example in Figure 2, misbonded Si or Ge atoms at the nanodot interfaces would result in the formation of nonshared valence electrons between atoms due a lack of covalent bonds between Si and Ge. The delocalized

electrons could hop to the conduction band or create polarization effects, which would help to keep the electrical conductivity. Note that previous studies showed that an increase of the number of charge carriers by doping (up to an optimal concentration due to the electronic λ) enables to increase ZT.[5,31]

It is still not so clear how the proposed weakly bonded supercrystal could be fabricated. Nevertheless, we could envision that the Si layer on which the Ge islands are grown could be prepatterned by either electron or ion beam lithography, ion implantation, or laser annealing, for instance (technologies being already used in microelectronics).[16,17,32−35] Experimentalists could then find a way to introduce a proper strain from the prepatterned Si. The strain should be exerted so that the Ge islands would grow on or move to out-of-equilibrium Si sites that do not lead to energy minimization. Weak bonds could be formed at the Si/Ge interfaces thereof.

CONCLUSIONS

An ultralow thermal conductivity is obtained in a Si/Ge supercrystal vs the number of weakly bonded Ge nanodots. When all nanodots are weakly bonded (i.e., $q = 1$), a fast λ diminution is first observed when d is increased until the ultralow minimum $\lambda^* = 0.009$ W/(m K) is reached. This λ value shows a $\sim$ 17 000-fold reduction compared with bulk Si, possibly leading to high ZT. A factor—as high as ~50-fold—accounts for the increase of q from 0 to 1 in the total λ decrease. Thereafter, when $d > d^* \approx 30$ nm, λ increases and passes Λ_{min} when $d \geq 500$ nm $= 5l_{Si}$. When q is decreased from 1 to 0, λ^* is augmented from 0.009 to 0.43 W/(m K), the last value being for a perfect crystal (i.e., $q = 0$). We also believe that it is not possible to beat Λ_{min} by a significant factor using other types of nanomaterials for which phonon blocking is only 1D or 2D instead of 3D in the proposed nanomaterial with weak bonds.

ASSOCIATED CONTENT

Supporting Information

Mathematical demonstration of eq 1. This material is available free of charge via the Internet at http://pubs.acs.org.

AUTHOR INFORMATION

Corresponding Author

*E-mail: jngillet@gmail.com.

Notes

The authors declare no competing financial interest.

ACKNOWLEDGMENTS

The author gratefully thanks the Jawaharlal Nehru Institute of Advanced Study, JNU.

REFERENCES

(1) Gillet, J.-N Marked thermal exaltation in hybrid thin membranous nanomaterials covered by stretched nanodots for thermoelectrics and passive cooling. *ACS Appl. Mater. Interfaces* **2010**, *2* (12), 3486−3492.

(2) Venkatasubramanian, R.; Siivola, E.; Colpitts, T.; O'Quinn, B. Thin-film thermoelectric devices with high room-temperature figures of merit. *Nature* **2001**, *413*, 597−602.

(3) Tritt, T. M.; Bottner, H.; Chen, L. Thermoelectrics: Direct solar thermal energy conversion. *MRS Bull.* **2008**, *33* (4), 366−368.

(4) Gillet, J.-N.; Chalopin, Y.; Volz, S. Atomic-scale three-dimensional phononic crystals with a very low thermal conductivity to design crystalline thermoelectric devices. *ASME J. Heat Transfer* **2009**, *131* (4), 043206.

(5) Toberer, E. S.; May, A. F.; Snyder, G. J. Zintl Chemistry for Designing High Efficiency Thermoelectric Materials. *Chem. Mater.* **2010**, *22* (3), 624−634.

(6) Lee, M. L.; Venkatasubramanian, R. Effect of nanodot areal density and period on thermal conductivity in SiGe/Si nanodot superlattices. *Appl. Phys. Lett.* **2008**, *92* (5), 053112.

(7) Gillet, J.-N. Weak Bonding Effect on the Ultralow Thermal Conductivity of Germanium Nanodot Arrays in Silicon. *Mater. Res. Soc. Symp. Proc.* **2012**, *1404*, DOI: 10.1557/opl.2012.343.

(8) Chalopin, Y.; Gillet, J.-N.; Volz, S. Predominance of thermal contact resistance in a silicon nanowire on a planar substrate. *Phys. Rev. B* **2008**, *77* (23), 233309.

(9) Hochbaum, A. I.; Chen, R.; Delgado, R. D.; Liang, W.; Garnett, E. C.; Najaran, M.; Majumdar, A.; Yang, P. Enhanced thermoelectric performance of rough silicon nanowires. *Nature* **2008**, *451*, 163−167.

(10) Cahill, D. G.; Watson, S. K.; Pohl, R. O. Lower limit to the thermal conductivity of disordered crystals. *Phys. Rev. B* **1992**, *46* (10), 6131−6140.

(11) Chiritescu, C.; Cahill, D. G.; Nguyen, N.; Johnson, D.; Bodapati, A.; Keblinski, P.; Zschack, P. Ultralow thermal conductivity in disordered, layered WSe_2 crystals. *Science* **2007**, *315*, 351−353.

(12) Chiritescu, C.; Cahill, D. G.; Heideman, C.; Lin, Q.; Mortensen, C.; Nguyen, N. T.; Johnson, D.; Rostek, R.; Bottner, H. Low thermal conductivity in nanoscale layered materials synthesized by the method of modulated elemental reactants. *J. Appl. Phys.* **2008**, *104* (3), 033533.

(13) Pernot, G.; Stoffel, M.; Savic, I.; Pezzoli, F.; Chen, P.; Savelli, G.; Jacquot, A.; Schumann, J.; Denker, U.; Monch, I.; Deneke, Ch.; Schmidt, O. G.; Rampnoux, J. M.; Wang, S.; Plissonier, M.; Rastelli, A.; Dilhaire, S.; Mingo, N. Precise control of thermal conductivity at the nanoscale through individual phonon-scattering barriers. *Nat. Mater.* **2010**, *9*, 491−495.

(14) Gillet, J.-N. Theoretical study of the ultralow thermal conductivity of weakly-bonded germanium quantum dot arrays in silicon. *Appl. Phys. Express* **2011**, *4*, 015201.

(15) Luo, L.; Rossell, M. D.; Xie, D.; Erni, R.; Niederberger, M. Microwave-assisted nonaqueous sol−gel synthesis: From Al:ZnO nanoparticles to transparent conducting Films. *ACS Sustainable Chem. Eng.* **2013**, *1* (1), 152−160.

(16) Guise, O.; Yates, J. T., Jr.; Levy, J.; Ahner, J.; Vaithyanathan, V.; Schlom, D. G. Patterning of sub-10-nm Ge islands on Si(100) by directed self-assembly. *Appl. Phys. Lett.* **2005**, *87* (17), 171902.

(17) Yakes, M. K.; Cress, C. D.; Tischier, J. G.; Bracker, A. S. Three-dimensional control of self-assembled quantum dot configurations. *ACS Nano* **2010**, *4* (7), 3877−3882.

(18) Jian, Z.; Kaiming, Z.; Xide, X. Modification of Stillinger-Weber potentials for Si and Ge. *Phys. Rev. B* **1990**, *41* (18), 12915−12918.

(19) He, J.; Sootsman, J. R.; Girard, S. N.; Zheng, J.-C.; Wen, J.; Zhu, Y.; Kanatzidis, M. G.; Dravid, V. P. On the origin of increased phonon scattering in Nanostructured PbTe based thermoelectric materials. *J. Am. Chem. Soc.* **2010**, *132* (25), 8669−8675.

(20) Glassbrenner, C. J.; Slack, G. A. Thermal conductivity of Silicon and Germanium from 3 K to the melting point. *Phys. Rev.* **1964**, *134* (4A), A1058−A1069.

(21) Gillet, J.-N.; Volz, S. Self-assembled germanium quantum-dot supercrystals in silicon with extremely low thermal conductivities for thermoelectrics. *J. Electron. Mater.* **2010**, *39* (9), 2154−2161.

(22) Majumdar, A. Microscale Heat Conduction in Dielectric Thin FilmsASME J. *Heat Transfer* **1993**, *115* (1), 7−16.

(23) Kim, W.; Majumdar, A. Phonon scattering cross section of polydispersed spherical nanoparticles. *J. Appl. Phys.* **2006**, *99* (8), 084306.

(24) van de Hulst, H. C. *Light Scattering by Small Particles*; Dover: New York, 1981.

(25) Bohren, C. F.; Huffman, D. R. *Absorption and Scattering of Light by Small Particles*; Wiley: New York, 1998.

(26) Gillet, J.-N.; Sheng, Y. Multiplexed computer-generated holograms with irregular-shaped polygonal apertures and discrete phase levels. *J. Opt. Soc. A* **2002**, *19* (12), 2403−2413.
(27) Gillet, J.-N; Sheng, Y. Multiplexed computer-generated holograms with polygonal-aperture layouts optimized by genetic algorithm. *Appl. Opt.* **2003**, *42* (20), 4156−4165.
(28) Gillet, J.-N.; Sheng, Y. Irregular spot array generator with trapezoidal apertures of varying heights. *Opt. Commun.* **1999**, *166* (1−6), 1−7.
(29) Lee, S.-M.; Cahill, D. G.; Venkatasubramanian, R. Thermal conductivity of Si−Ge superlattices. *Appl. Phys. Lett.* **1997**, *70* (22), 2957−2959.
(30) Thanh, V. L.; Yam, V. Superlattices of self-assembled Ge/Si(0 0 1) quantum dots. *Appl. Surf. Sci.* **2003**, *212*−*213*, 296−304.
(31) Yu, J.-K.; Mitrovic, S.; Tham, D.; Varghese, J.; Heath, J. R. Reduction of thermal conductivity in phononic nanomesh structures. *Nat. Nanotechnol.* **2012**, *5*, 718−721.
(32) Rastelli, A.; Stoffel, M.; Katsaros, G.; Tersoff, J.; Denker, U.; Merdzhanovaa, T.; Kar, G. S.; Costantini, G.; Kerna, K.; von Kanel, H.; Schmidt, O. G. Reading the footprints of strained islands. *Microelectronics J.* **2006**, *37* (12), 1471−1476.
(33) Ieong, M.; Doris, B.; Kedzierski, J.; Rim, K.; Yang, M. Silicon device scaling to the sub-10-nm regime. *Science* **2004**, *306*, 2057−2060.
(34) Gillet, J.-N.; Degorce, J.-Y.; Meunier, M. General model and segregation coefficient measurement for ultrashallow doping by excimer laser annealing. *Appl. Phys. Lett.* **2005**, *86* (22), 222104.
(35) Degorce, J.-Y.; Gillet, J.-N.; Magny, F.; Meunier, M. Three-dimensional transient temperature field model for laser annealing. *J. Appl. Phys.* **2005**, *97* (3), 033520.